Coronary Arterial Stents: Safety and Artifacts during MR Imaging[1]

Jürgen Hug, MD
Eike Nagel, MD
Axel Bornstedt, PhD
Bernhard Schnackenburg, PhD
Helmut Oswald, PhD
Eckart Fleck, MD

Index terms:
Coronary vessels, MR, 54.121411, 54.121412, 54.121416,
Coronary vessels, stents and prostheses, 54.126
Magnetic resonance (MR), artifact, 54.121411, 54.121412, 54.121416
Magnetic resonance (MR), rapid imaging, 54.121411, 54.121412, 54.121416,
Magnetic resonance (MR), safety, 54.121411, 54.121412, 54.121416

Radiology 2000; 216:781–787

Abbreviations:
B_0 = constant magnetic induction field
TFE = turbo field echo
TSE = turbo spin echo

[1] From the Department of Internal Medicine and Cardiology, Charité, Campus Virchow-Klinikum Humboldt University & German Heart Institute, Augustenburger Platz 1, 13353 Berlin, Germany (J.H., E.N., A.B., H.O., E.F.), and Philips Medical Systems, Hamburg, Germany (B.S.). Received December 28, 1998; revision requested February 23, 1999; final revision received November 16; accepted December 6. **Address correspondence to** J.H. (e-mail: *Juergen.hug@charite.de*).

Author contributions:
Guarantor of integrity of entire study, J.H.; study concepts, J.H.; study design, E.N., J.H.; definition of intellectual content, E.N., J.H.; literature research, H.O.; clinical studies, J.H.; experimental studies, E.N., J.H.; data acquisition, B.S.; data analysis, H.O., B.S.; statistical analysis, H.O., A.B.; manuscript preparation, J.H.; manuscript editing, E.N., J.H.; manuscript review, E.F.

PURPOSE: To investigate the safety and imaging artifacts with different coronary arterial stents and magnetic resonance (MR) imaging sequences.

MATERIALS AND METHODS: The heating, artifacts, and ferromagnetism with different stents were studied with a 1.5-T MR tomograph with ultrafast gradients by using turbo spin-echo, turbo gradient-echo, and echo-planar imaging sequences. Nineteen stents, which were 8–25 mm in length and 3.0–4.5 mm in diameter, were evaluated. Stent deviation induced by the magnetic field and during MR imaging, migration, and heating caused by the radio-frequency pulses were examined. The size of imaging artifacts was measured with all the stents under standardized conditions and with six stents after their implantation into the coronary arteries of freshly explanted pig hearts.

RESULTS: All except two types of stents showed minimal ferromagnetism. No device migration or heating was induced. Turbo spin-echo images had minimal artifacts; larger artifacts were seen on the turbo gradient-echo and echo-planar images. With ultrafast gradients, the artifacts on the echo-planar images were substantially reduced.

CONCLUSION: The studied coronary stents were not influenced by heating or motion during 1.5-T MR imaging. Artifact size differed according to the type and size of the stent and the MR imaging sequence used. Thus, patients with these stents can be safely examined.

Cardiovascular disease remains the leading cause of morbidity and mortality in the industrialized world. To improve the immediate and long-term results of balloon-assisted angioplasty, there has been a quest for new forms of catheter-based therapies that has resulted in the development of an assortment of new devices, such as the coronary arterial stent (1,2). Since the introduction of coronary arterial stents (3), coronary stent placement has taken the lead in the treatment of obstructive coronary arterial disease. Coronary arterial stents are typically made of stainless steel or tantalum. After implantation into the artery, they are endothelialized and incorporated into the vessel wall.

Magnetic resonance (MR) imaging has become an important tool for imaging many internal organs, including the heart (4,5). Cardiac MR imaging has been shown to provide accurate images of the proximal and medial parts of the coronary arteries (6–9) and to be highly superior to stress echocardiography for the detection of ischemic heart disease (10). Thus, more and more patients, especially those with coronary arterial disease, can be expected to undergo MR imaging examinations. Because of the strong magnetic field required for current imaging systems, there has been concern with regard to the possible heating or dislocation of previously implanted coronary stents in patients scheduled for MR imaging investigations. It has been recommended that patients with coronary stents should wait several weeks after stent implantation before they undergo MR imaging. In addition, the implanted stents can cause imaging artifacts at the implantation site that prohibit the visualization of underlying structures.

This study was performed to examine the occurrence of ferromagnetism in coronary arterial stents as a cause of movement, determine possible heating during MR imaging, and measure the size of susceptibility artifacts caused by the different stents.

TABLE 1
Coronary Arterial Stents Studied for Ferromagnetism, Heating, and Imaging Artifacts

Stent*	Vendor†	Length (mm)	Diameter (mm)
ACS MULTI-LINK RX DUET	Guidant	8	3.5
ACS MULTI-LINK RX DUET	Guidant	18	3.0
ACS RX MULTI-LINK	Guidant	15	3.0
ACS RX MULTI-LINK	Guidant	15	4.0
ACS RX MULTI-LINK	Guidant	25	3.0
Micro Stent II	Medtronic AVE	24	3.0
Bard XT	Bard Interventional Products	15	3.0
BeStent	Medtronic AVE	15	3.0
BeStent	Medtronic AVE	25	3.0
Giantourco-Roubin II	Cook	20	3.0
InFlow	InFlow Dynamics	15	3.0
InFlow Gold	InFlow Dynamics	9	3.0
InFlow Gold	InFlow Dynamics	15	3.0
MAC-Stent	AMG	17	3.0
Palmaz-Schatz	Johnson & Johnson	15	3.5
R-Stent	Spectranetics	16	3.0
Seaquence	Nycomed Amersham	15	3.5
Wallstent	Schneider	23	4.5
Wiktor GX	Medtronic AVE	15	4.0

*Inflow Gold stents are composed of 316 low-carbon stainless steel with a gold plate. The Wallstent is composed of a cobalt-based alloy with a platinum core. The Wiktor GX stent is composed of tantalum. All of the remaining stents are composed of 316 low-carbon stainless steel.

† Vendor locations: AMG (Angewandte Medizin- und Gesundheitstechnik), Munich, Germany; Guidant, Austin, Tex; Bard Interventional Products, Billerica, Mass; Cook, Bloomington, Ind; InFlow Dynamics, Munich, Germany; Johnson & Johnson, Miami Lakes, Fla; Medtronic AVE, Minneapolis, Minn; Nycomed Amersham, Princeton, NJ; Schneider, Minneapolis, Minn; Spectranetics, Colorado Springs, Colo.

MATERIALS AND METHODS

Devices Studied

Nineteen coronary arterial stents of different length, size, and material from 10 different manufacturers were studied. Detailed descriptions of the stents are listed in Table 1. All of the stents were composed of 316 low-carbon stainless steel, except the Wiktor stent, which is made of tantalum, and the Wallstent, which is made of a cobalt-based alloy with a platinum core. The InFlow Gold device is a stainless steel stent coated with a thin layer of gold.

MR Imaging

All MR imaging studies were performed by using a Gyroscan ACS NT 1.5-T MR tomograph (Philips Medical Systems, Best, the Netherlands) with an ultrafast gradient system, which could be set to regular or ultrafast gradients, depending on the MR imaging study planned. The regular gradients allowed a slew rate of 16.7 T/m/sec and a maximum magnetic field gradient of 10 mT/m, whereas the ultrafast gradients allowed a slew rate of 100 T/m/sec and a maximum magnetic field gradient of 21 mT/m. Similar MR imaging sequences, such as those routinely used for clinical cardiac MR imaging, as well as high-energy MR imaging sequences with ultrafast gradients, which are currently mainly used by research sites for the evaluation of new cardiac MR imaging capabilities, such as perfusion measurements or coronary arterial imaging, were applied to assess the ferromagnetism, possible movement and heating, and size of imaging artifacts of the devices. The following MR sequences were used with the regular gradients: turbo spin echo (TSE, segmented k-space spin echo), turbo field echo (TFE, segmented k-space spoiled gradient echo), and echo-planar imaging. For high-energy MR imaging with the ultrafast gradient systems, fast TFE and fast echo-planar imaging sequences were used. The section thickness varied between 4 mm (TFE), 8.0 mm (echo-planar imaging), and 10.0 mm (TSE), with intersection gaps of 0 mm (TFE), 0.8 mm (echo-planar imaging), and 1.0 mm (TSE). One of the study objectives was to compare MR imaging sequences that are routinely used for clinical cardiac MR imaging. We routinely use a TSE MR imaging sequence with a larger section thickness of 10 mm to identify anatomic structures. For this reason, we stayed with the 10-mm section thickness although we knew that it could result in smaller artifact sizes owing to a greater partial volume effect. The field of view for all the sequences was 300 mm, and depending on the acquisition matrix (128×128 or 256×256), the in-plane image resolution varied between 2.3×2.3 and 1.2×1.2 mm. Details about the different MR imaging sequences are listed in Table 2.

Determination of Device Ferromagnetism and Movement

A method previously described by New et al (11) and Scott and Pettigrew (12) was modified to measure the occurrence of ferromagnetism. All stents, except the self-expandable Wallstent, were expanded to their nominal diameter with a percutaneous transluminal coronary angioplasty balloon. A thin suture material was tied to the longitudinal middle portion of each stent, which was then horizontally suspended. Possible deflection and motion caused by the magnetic field of the 1.5-T MR imaging tomograph were determined in the region of the largest magnetic field heterogeneity at the entrance of the bore of the MR imaging magnet and during imaging with the different sequences. The angle of deflection from the vertical together with the alignment of the longitudinal axis were determined with a protractor. The magnitude of the magnetic force vector applied to the device was indicative of the magnitude of ferromagnetism induced by the magnet. The force (F, in newtons) was calculated by using the formula $F = m \cdot g \cdot \tan\theta$, where m is the mass of the device (in kilograms); g, the gravitational acceleration (9.81 m/sec^2); and $\tan\theta$, the deflection angle from the vertical.

TABLE 2
MR Imaging Sequences Used to Determine Ferromagnetism, Heating, and Imaging Artifacts

MR Sequence	TE (msec)	TR (msec)	FOV (mm)	Section Thickness (mm)	Matrix (Pixels)*
TSE	11.0	750.0	300	10	256 × 256
TFE†	8.2	13.6	300	4	256 × 256
Fast TFE‡	6.9	10.8	300	4	256 × 256
EPI§	12.1	750.0	300	8	128 × 128
Fast EPI‡	5.9	750.0	300	8	128 × 128

Note.—EPI = echo planar imaging, FOV = field of view, TE = echo time, TFE = turbo field echo, TR = repetition time.
* The in-plane image resolution was 1.2 × 1.2 mm for the 256 × 256 matrix and 2.3 × 2.3 mm for the 128 × 128 matrix.
† K-space segmentation (16 segments) and a flip angle of 60° were used for the TFE sequence.
‡ Fast TFE and fast EPI sequences were performed with ultrafast gradients (gradient field strength, 21 mT/m; slew rate, 100 T/m/sec).
§ The EPI factor was 7 and the flip angle was 30° for the EPI sequences.

The control device was a stainless-steel needle (Ethicon Mersilene EH7637 [mass 159 mg]; Johnson & Johnson, Miami Lakes, Fla) suspended and similarly placed into the magnetic field. The devices that demonstrated ferromagnetism were further evaluated for possible magnetically induced device movement. The position of each stent was marked on a millimeter grid, and the possible movement induced during the different MR imaging sequences was measured as a distance in millimeters.

Determination of Device Heating

To determine possible heating, the fully expanded stents were placed at room temperature into a homogeneous medium and positioned in the 1.5-T MR imaging tomograph parallel to the magnetic radio-frequency field. A pot of stirred low-fat (3.5%) plain yogurt was chosen as the homogeneous medium. The composition of the yogurt per 150 g was as follows: protein, 7.7 g; carbohydrates, 11.0 g; fat, 1.2 g; calcium, 285 mg; phosphorus, 240 mg; and minor concentrations of some other nutrients. This medium was chosen for two reasons: first, because the T1 of 1,045 msec and T2 of 160 msec that were used for the yogurt were nearly comparable to the relaxation times of human myocardial tissue and second, for practical reasons. Placement of the tiny, fully expanded stents deep into the medium in a fixed and stable position was possible without any damage. For extreme in vitro worst-case experiments and testing of possible heating, the stents were imaged for 30 minutes by using a TSE sequence with an echo train consisting of nine 180° pulses (field of view, 385 mm; matrix, 256 × 256; section thickness, 10 mm). In addition, three saturation sections were used to achieve a maximum of adjustable radio-frequency power and thus yield a specific absorption rate of 3.9 W per kilogram of body weight. (The maximum specific absorption rate allowed in human studies is 4.0 W/kg.)

Changes in the temperature of the stents or adjacent medium were detected by obtaining continuous temperature measurements during exposure with a carefully calibrated fiberoptic temperature probe (model FT705; IRE-Polus, Moscow, Russia) placed into the expanded lumen of the stent in close contact with the stent wall. The accuracy of the temperature measurements was within 0.1°C. Heating of the temperature probe itself owing to power absorption, which would have resulted in false temperature measurements, was avoided by obtaining continuous measurements in a separate volume of the medium that did not contain stents. The measurements began after the stents were placed, and the homogeneous medium was thermally equilibrated with the ambient temperature.

MR Imaging of Stents and Artifacts

Susceptibility related signal loss is a term used (13) to refer to an artifact on MR images that consists of a region of signal void with a surrounding area of increased signal intensity that appears to be considerably larger than the actual size of the device that is causing the artifact. The presence and degree of MR imaging susceptibility artifacts caused by the coronary stents during the different sequences were evaluated under different conditions: (*a*) To determine the influence of the orientation of the fully expanded stents in the magnetic field on the size and shape of the imaging artifacts, three devices—the 24-mm Micro Stent II, 20-mm Giantourco-Roubin II stent, and 15-mm Palmaz-Schatz stent—were studied (by J.H., E.N., and B.S. in consensus) at different positions and orientations within the magnetic field. The position and orientation that caused the maximum artifact size were recorded. To obtain a maximum artifact size, all further studies were then performed with the stents in that position and orientation. (*b*) To standardize the conditions for measuring the expected imaging artifacts, the stents were fully expanded to their nominal diameter in the homogeneous yogurt medium that had a T1 of 1,045 msec and T2 of 160 msec, which resembled the in vivo relaxation times of myocardial tissue, and imaged at identical positions and orientations within the magnetic field. (*c*) To simulate in vivo conditions, six of the stents—the 18-mm DUET; 15-mm-long, 3.0-mm-diameter MULTI-LINK; 15-mm InFlow, 15-mm InFlow Gold, 15-mm Palmaz-Schatz, and 15-mm Wiktor GX devices—were implanted into the coronary arteries of three freshly explanted pig hearts by using standard angioplasty techniques. After placement of a guiding catheter into the coronary ostium, the premounted stents were implanted over a guide wire into the proximal coronary segments with balloon inflation up to 12 atm. Optimal placement of the implanted stents was controlled by means of selective coronary angiography.

After imaging with the regular (TSE, TFE, and echo-planar) and ultrafast (fast TFE and fast echo-planar) MR sequences was performed, the maximum artifact length (L) and maximum artifact diameter in two planes perpendicular to each other (D_1 and D_2) were determined. The artifact volume V was calculated on the basis of the formula $V = (\pi/4) \cdot D_1 \cdot D_2 \cdot L$.

Statistical Analyses

The results were expressed as single values or as the mean ± SD. One-way

analysis of variance was used to compare the results of the different MR imaging sequences, and in cases of overall significance, group differences were evaluated by using the Bonferroni modified *t* test. Least-squares linear regression was used to compare the MR imaging stent artifact lengths with the actual stent lengths. A *P* value of less than .05 was considered to be indicative of statistical significance.

RESULTS

Ferromagnetism and Device Migration

Of the 19 coronary arterial stents evaluated, two—the 8-mm DUET and the Wiktor GX—showed no ferromagnetism (Table 3). All of the other stents were mildly deflected by the magnetic field at the bore entrance of the magnet. The measured deflection angles ranged from 1° to 3°. Depending on the mass of the individual stent, the calculated ferromagnetic forces ranged from 2.3×10^{-6} to 27.6×10^{-6} N. No alignment of the stent with the magnetic field along its longitudinal axis was observed. In none of the stents was device movement induced by MR imaging with either regular or ultrafast gradients. In contrast, the needle used as the control device aligned its longitudinal axis along the longitudinal direction of the magnetic field and was maximally deflected by 80° at the bore entrance of the magnet; this resulted in a ferromagnetic force of 8.9×10^{-3} N.

Heating

During the 30 minutes of MR imaging no temperature changes in either the 19 coronary stents or the adjacent homogeneous medium were observed, even when high-energy dissipation sequences were used. The mean temperature before the start of MR imaging was 19.35°C ± 0.49, and at the end of the 30 minutes of MR imaging, it was 19.34°C ± 0.40. No change in temperature was found when only the fiberoptic probe without stents was placed in the medium and exposed to the same conditions.

Imaging Artifacts

All 19 stents created a substantial degree of artifacts. The artifact shapes and sizes differed substantially, depending on the orientation of the stents in the magnetic field. The biggest artifacts were observed when the position of the stents was perpendicular to the constant magnetic induction field (B_0), and the smallest artifacts were parallel to the static magnetic field. Figure 1 shows sagittal and transverse images of a large imaging artifact created by a 15-mm InFlow stent implanted into a freshly explanted pig heart and imaged with an echo-planar imaging sequence (repetition time msec/echo time msec, 750.0/12.1; echo-planar imaging factor, 7).

The shape of the observed imaging artifacts was always cylindrical, with the major extension parallel to the longitudinal axis of the expanded stent and a smaller extension perpendicular to the longitudinal axis. The size of the imaging artifacts differed according to the type and size of the implanted stent. As expected, the longer and larger coronary arterial stents created larger artifacts, whereas the smaller stents caused small artifacts (Fig 2). The measured artifact length was always longer than the actual stent length, but it never exceeded the length of the stent by 1 cm. With all MR imaging sequences, the artifact length correlated well with the actual stent length ($r = 0.92$ for the TSE sequence). As expected, the degree of susceptibility to produce artifacts varied according to the MR imaging sequence. The image quality of the TSE images was hardly affected; however, significantly larger artifacts were found on the TFE images, and even larger ones were seen on the echo-planar images ($P < .05$) (Fig 3). With the ultrafast gradient system, the large imaging artifacts produced with the regular echo-planar imaging sequence could be significantly reduced by using the fast echo-planar imaging sequence ($P < .01$) (Fig 3). No significant differences were found between the measurements of artifact size obtained under standardized conditions and those obtained after implantation of the stents into the coronary arteries of freshly explanted pig hearts.

TABLE 3
Coronary Arterial Stents: Ferromagnetic Force and Device Movement

Device/Length × Diameter (mm)	Mass (mg)	Ferromagnetic Force at 1.5 T (N)
DUET/8 × 3.5	10.8	0
DUET/18 × 3.0	26.0	8.9 E-06
MULTI-LINK RX/15 × 3.0	12.9	4.4 E-06
MULTI-LINK RX/15 × 4.0	13.1	2.3 E-06
MULTI-LINK RX/25 × 3.0	22.2	4.4 E-06
Micro Stent II/24 × 3.0	53.6	27.6 E-06
Bard XT/15 × 3.0	28.2	14.5 E-06
BeStent/15 × 3.0	14.9	5.1 E-06
BeStent/25 × 3.0	20.8	3.6 E-06
Gianturco-Roubin II/20 × 3.0	20.2	6.9 E-06
InFlow/15 × 3.0	16.4	8.4 E-06
InFlow Gold/9 × 3.0	17.0	2.9 E-06
InFlow Gold/15 × 3.0	26.4	9.0 E-06
MAC-Stent/17 × 3.0	14.6	5.0 E-06
Palmaz-Schatz/15 × 3.5	15.1	2.5 E-06
R-Stent/16 × 3.0	19.7	2.5 E-06
Seaquence/15 × 3.5	20.5	7.0 E-06
Wallstent/23 × 4.5	37.9	13.0 E-06
Wiktor GX/15 × 4.0	21.8	0

Note.—There was no device migration with any stent.

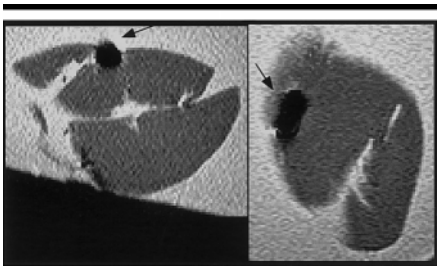

Figure 1. Transverse (left) and sagittal (right) MR images of an artifact (arrows) that was created by a 15-mm InFlow stent implanted in a freshly explanted pig heart and imaged with an echo-planar sequence (750.0/12.1; echo-planar imaging factor, 7), which caused the largest artifacts.

DISCUSSION

In the current study, it was shown that no substantial side effects, such as device migration or heating of coronary arterial stents, are induced by MR imaging, even when ultrafast gradient systems are used.

MR imaging is considered to be contraindicated in patients with ferromagnetic implants, primarily because of the potential risks associated with their possible movement, the induction of an electrical current, the potential for excessive heating, and the possibility of misinterpretation of an artifact produced by the presence of the object (11,14,15). Several factors influence the relative risk of MR imaging in patients with metallic implants: (*a*) the strength of the static magnetic field and of the gradients, (*b*) the degree of ferromagnetism in the implanted device, (*c*) the geometry of the implanted material, and (*d*) the location and orientation of the implant in situ during MR imaging (16). These factors should be carefully considered, particu-

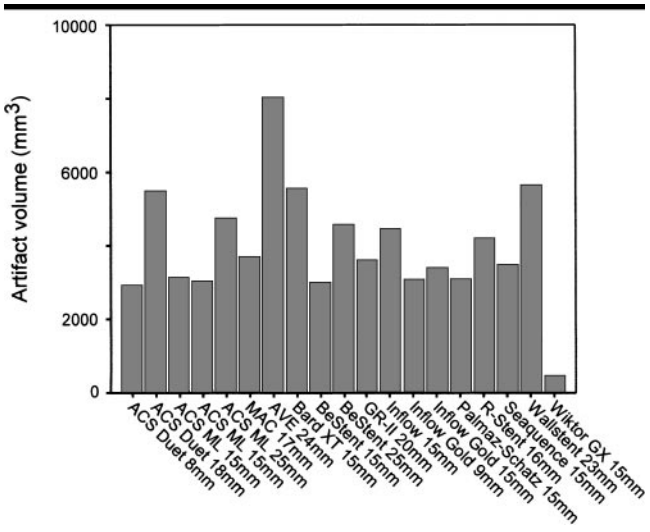

Figure 2. Graph illustrates the volumes (in mm^3) of the coronary arterial stent artifacts after imaging at 1.5 T with an echo-planar imaging sequence. The individual stents create different artifact volumes, depending on the stent type, material, and size. *ACS* = Austin Computer Systems, *GR* = Gianturco-Roubin, *ML* = MULTI-LINK.

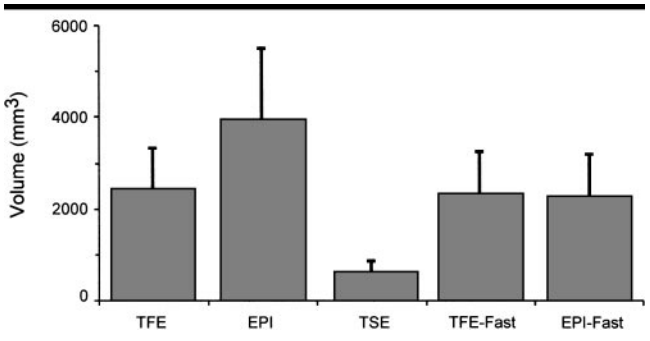

Figure 3. Graph illustrates the volumes (in means ± SD) of the coronary arterial stent artifacts, depending on the MR imaging sequence used. The TFE and echo-planar imaging (*EPI*) sequences caused significantly larger artifacts than did the TSE sequence ($P < .05$). Note that with the ultrafast echo-planar imaging (*EPI-Fast*) gradients, the large artifact volumes seen on the EPI images were significantly reduced ($P < .01$). *TFE-Fast* = ultrafast TFE.

larly if the implanted object is located in a potentially dangerous area of the body, such as near a vascular structure where migration or heating could severely injure the patient (17,18).

Ferromagnetism and Device Migration

The highest ferromagnetic force was found in the stents with the greatest mass. No ferromagnetism was observed in the stent with the lowest mass—the 8-mm DUET—or in the 15-mm Wiktor GX stent, which was the only device in the study made from tantalum. Several studies have involved assessment of the ferromagnetic qualities of various metallic implants (14), materials (19–22), or devices, such as aneurysm or hemostatic clips (23–25), carotid arterial vascular clamps (26), dental devices (11), heart valve prostheses (26–28), intravascular coils and filters (29,30), ocular implants (31), and vascular access ports (31–33). The authors of these studies concluded that patients with metallic implants can be examined safely with MR imaging, providing that the objects either are not ferromagnetic or are minimally ferromagnetic—that is, the deflection force is insufficient to move or dislodge the implant in situ.

In the current study, it was shown that minimum ferromagnetism may occur in most of the evaluated stents. However, the ferromagnetic force experienced during a 1.5-T MR imaging examination is too small to cause migration of the stent. In addition, the forces applied to a stent implanted into the coronary arteries owing to rapid motion, with acceleration and deceleration of the heart during cardiac contraction and relaxation, are expected to be much higher than those caused by the magnetic field (34).

Heating

Because the fully expanded stents are closed loops, it should be determined whether, with the changing magnetic field strength associated with the rapidly pulsed gradients used in MR imaging, a current could be induced and cause local heating (35). Pulsed radio-frequency fields and time-dependent gradient fields could be possible sources of such heating effects. However, in this study, no heating effects were observed during the MR imaging of any of the 19 coronary arterial stents. The degree of radio-frequency energy imposed on the stents in the current study was among the highest that can be achieved with current imaging units and normally is not used for routine MR imaging examinations. Most MR imaging units that are used clinically have lower magnetic field strengths and slower gradient systems and thus are associated with an even smaller risk of induced heating. However, with continuous progress in MR imaging technology, even faster gradient systems that allow higher spatial resolution and less imaging time and that minimize motion artifacts are being developed and introduced into clinical practice.

The determination of possible heating effects with an MR imaging tomograph is complex, because heating may be very localized and standard measurement systems cannot be used to detect minimum temperature changes. Heating measurements can be performed with different devices, such as a thermocouple, an infrared camera, or a fiberoptic temperature probe. The advantage of the fiberoptic probe used in this study was that continuous temperature measurement during exposure was possible. In our experiments, we were able to rule out the possibility of the fiberoptic probe acting like an antenna and absorbing power, which could have caused false measurements and the medium to heat. However, one cause of error with a fiberoptic probe could be that only localized temperature measurements at the tip of the probe in close contact with the stents and the adjacent medium can be performed. In ad-

dition, heating may occur with one particular radio-frequency pulse at one particular position within the imaging unit but not under minimally different conditions. Thus, the possible heating of a device could not be completely excluded in our measurements.

Theoretically, heating is caused by the radio-frequency energy of the MR imaging tomograph. If the resonance length ($\lambda/2$ or $\lambda/4$) is achieved, the interaction between the radio-frequency energy and the conducting material may produce an electric field, which can introduce electric currents. These small electric currents can be potential causes of heating. However, in addition to our measurements, which were performed with a maximum degree of radio-frequency energy, from a theoretical standpoint, the temperature changes caused by MR imaging of small metallic objects appear to be negligible (36). Coronary arterial stents are too small to reach the resonance length needed to induce an electric current.

Artifacts

MR imaging artifacts are magnetic susceptibility artifacts caused by local magnetic field changes that are produced by the ferromagnetic, paramagnetic, and diamagnetic properties of the metallic devices (37). The mechanism of artifact production and the mechanism of image distortion are the same in these devices. Usually, there is good correlation between the ferromagnetic properties of a device and the size of the expected imaging artifacts. However, there can also be a divergence between the ferromagnetism of a device and the size of the produced imaging artifacts (37), as seen in our study of coronary arterial stents, which caused moderate MR imaging artifacts despite their lack of strong ferromagnetism.

The cause of imaging artifacts with nonferromagnetic metallic devices is thought to be a reduction in radio-frequency amplitude near the device, which depends on its shape (38). These effects are most pronounced at the regions of greatest magnetic field heterogeneity, and radio-frequency amplitude changes are most pronounced close to the edges and points of the metallic surface of the implants. The orientation of the major extent of the artifact of these nonferromagnetic devices is parallel to the frequency-encoding gradient direction (39). The B_0 induces a dipole field in the stent, which changes the B_0 (40). The shape of this B_0 perturbation is determined by the relative orientation of the stent to the B_0. The size of the B_0 perturbation is maximized if the stent is oriented parallel to the B_0.

The properties of 316 low-carbon stainless steel, the material with which most currently available stents are made, have been previously reviewed (11). This steel alloy is austenitic and nonmagnetic. However, the type of manufacturing used to create the complex shapes of coronary arterial stents may produce ferromagnetic properties within the stent. Compared with 304 low-carbon stainless steel, the 316 low-carbon variety has a higher nickel content (10%–14% versus 8%–12% in the 304 low-carbon variety). The nickel stabilizes the iron in a nonmagnetic state and therefore diminishes the occurrence of ferromagnetism in stents composed of 316 low-carbon stainless steel.

Because artifact size depends mainly on the geometry and composition of the stent material, voxel size is expected to have a minor effect on artifact size. With the typical in-plane resolution and section thickness used in this study, we expected a maximum error in length measurement of ± 1 pixel at comparison among the different sequences.

As expected, the largest artifacts were observed with the echo-planar and TFE imaging sequences. One reason for the smaller artifacts with the TSE sequences could be the larger section thickness that was used. The 10-mm section thickness used in TSE imaging could have resulted in a smaller artifact size because of a greater partial volume effect. With the use of ultrafast gradients, the actual echo time was reduced, and this resulted in substantially smaller artifact sizes, especially with the echo-planar imaging sequences. With ongoing progress in MR imaging technology, shorter echo times, and thus further reductions in artifacts caused by stents, will be possible in the future.

In summary, our study results demonstrate that the evaluated coronary arterial stents are not significantly influenced by the 1.5-T magnetic field used in clinical MR imaging studies. No motion or heating effects were observed. A possible explanation is the relatively minor ferromagnetic nature of the stent materials, as well as the low mass and size of the devices, which results in minimal magnetic force being exerted on the stents. Coronary arterial stents generate susceptibility artifacts that extend in excess of the true size of the stents and make imaging of the underlying structures impossible. Artifact size differs according to the type and size of the stent and the MR imaging sequence used; the larger artifacts are seen with the larger and longer stents and with echo-planar imaging sequences. MR imaging of coronary arteries does not influence the regions beyond approximately 1 cm from the implantation site. Thus, routine MR imaging at 1.5 T with regular or ultrafast gradients does not induce motion or heating of the evaluated coronary arterial stents.

References

1. Waller B. "Crackers, breakers, stretchers, drillers, scrapers, shavers, burners, welders and melters": the future treatment of atherosclerotic coronary artery disease?—a clinical-morphologic assessment. J Am Coll Cardiol 1989; 13:969–987.
2. de Jaegere P, de Feyter P, van der Giessen W, Serruys P. Endovascular stents: preliminary clinical results and future developments. Clin Cardiol 1993; 16:369–378.
3. Sigwart U, Puel J, Mirkovitch V, Joffre F, Kappenberger L. Intravascular stents to prevent occlusion and restenosis after transluminal angioplasty. N Engl J Med 1987; 316:701–706.
4. Pettigrew R. Dynamic magnetic resonance imaging in acquired heart disease. Semin Ultrasound CT MR 1991; 12: 61–91.
5. Nienaber C, von Kodolitsch Y, Nicolas V, et al. The diagnosis of thoracic aortic dissection by noninvasive imaging procedures. N Engl J Med 1993; 328:1–9.
6. Goldfarb JW, Edelman RR. Coronary arteries: breath-hold, gadolinium-enhanced, three-dimensional MR angiography. Radiology 1998; 206:830–834.
7. Pennell DJ, Bogren HG, Keegan J, Firmin DN, Underwood SR. Assessment of coronary artery stenosis by magnetic resonance imaging. Heart 1996; 75:127–133.
8. Kessler W, Achenbach S, Moshage W, et al. Usefulness of respiratory gated magnetic resonance coronary angiography in assessing narrowings > or = 50% in diameter in native coronary arteries and in aortocoronary bypass conduits. Am J Cardiol 1997; 80:989–993.
9. Post JC, van Rossum AC, Hofman MB, Valk J, Visser CA. Three-dimensional respiratory-gated MR angiography of coronary arteries: comparison with conventional coronary angiography. AJR Am J Roentgenol 1996; 166:1399–1404.
10. Nagel E, Lehmkuhl H, Bocksch W, et al. Noninvasive diagnosis of ischemia-induced wall motion abnormalities with the use of high-dose dobutamine stress MRI: comparison with dobutamine stress echocardiography. Circulation 1999; 99: 763–770.
11. New P, Rosen B, Brady T, et al. Potential hazards and artifacts of ferromagnetic and nonferromagnetic surgical and dental materials and devices in nuclear magnetic resonance imaging. Radiology 1983; 147:139–148.
12. Scott N, Pettigrew R. Absence of movement of coronary stents after placement in a magnetic resonance imaging field. Am J Cardiol 1994; 73:900–901.
13. Bernardino M, Steinberg H, Pearson T, Gedgaudas-McClees R, Torres W, Hender-

son J. Shunts for portal hypertension: MR and angiography for determination of patency. Radiology 1986; 158:57–61.
14. Shellock F, Crues J. High-field-strength MR imaging and metallic biomedical implants: an ex vivo evaluation of deflection forces. AJR Am J Roentgenol 1988; 151:389–392.
15. Shellock F. Biological effects and safety aspects of magnetic resonance imaging. Magn Reson Q 1989; 5:243–261.
16. Teitelbaum GP, Yee CA, Van Horn DD, Kim HS, Colletti PM. Metallic ballistic fragments: MR imaging safety and artifacts. Radiology 1990; 175:855–859.
17. Shellock F, Kanal E. Policies, guidelines, and recommendations for MR imaging and patient management: SMRI Safety Committee. J Magn Reson Imaging 1991; 1:97–101.
18. Kanal E, Shellock F, Talagala L. Safety considerations in MR imaging. Radiology 1990; 176:593–606.
19. Leon J, Gabriele O. Middle ear prosthesis: significance in magnetic resonance imaging. Magn Reson Imaging 1987; 5:405–406.
20. Mark A, Hricak H. Intrauterine contraceptive devices: MR imaging. Radiology 1987; 162:311–314.
21. Shellock F, Shellock V. Ceramic surgical instruments: ex vivo evaluation of compatibility with MR imaging at 1.5 T. J Magn Reson Imaging 1996; 6:954–956.
22. Fagan LL, Shellock FG, Brenner RJ, Rothman B. Ex vivo evaluation of ferromagnetism, heating, and artifacts of breast tissue expanders exposed to a 1.5-T MR system. J Magn Reson Imaging 1995; 5:614–616.
23. Barrafato D, Henkelman R. Magnetic resonance imaging and surgical clips. Can J Surg 1984; 27:509–10, 512.
24. Dujovny M, Kossovsky N, Kossowsky R, et al. Aneurysm clip motion during magnetic resonance imaging: in vivo experimental study with metallurgical factor analysis. Neurosurgery 1985; 17:543–548.
25. Shellock F, Kanal E. Aneurysm clips: evaluation of MR imaging artifacts at 1.5 T. Radiology 1998; 209:563–566.
26. Teitelbaum GP, Lin MC, Watanabe AT, Norfray JF, Young TI, Bradley WG Jr. Ferromagnetism and MR imaging: safety of carotid vascular clamps. AJNR Am J Neuroradiol 1990; 11:267–272.
27. Hassler M, Le Bas J, Wolf J, Contamin C, Waksmann B, Coulomb M. Effects of the magnetic field in magnetic resonance imaging on 15 tested cardiac valve prostheses. J Radiol 1986; 67:661–666.
28. Soulen R, Budinger T, Higgins C. Magnetic resonance imaging of prosthetic heart valves. Radiology 1985; 154:705–707.
29. Teitelbaum G, Bradley WG Jr, Klein B. MR imaging artifacts, ferromagnetism, and magnetic torque of intravascular filters, stents, and coils. Radiology 1988; 166: 657–664.
30. Marshall M, Teitelbaum G, Kim H, Develkis J. Ferromagnetism and magnetic resonance artifacts of platinum embolization microcoils. Cardiovasc Intervent Radiol 1991; 14:163–166.
31. Zheutlin J, Thompson J, Shofner R. The safety of magnetic resonance imaging with intraorbital metallic objects after retinal reattachment or trauma. Am J Ophthalmol 1987; 103:831.
32. Shellock F, Nogueira M, Morisoli S. MR imaging and vascular access ports: ex vivo evaluation of ferromagnetism, heating, and artifacts at 1.5 T. J Magn Reson Imaging 1995; 5:481–484.
33. Shellock F, Shellock V. Vascular access ports and catheters: ex vivo testing of ferromagnetism, heating, and artifacts associated with MR imaging. Magn Reson Imaging 1996; 4:443–447.
34. Hofman MB, Wickline SA, Lorenz CH. Quantification of in-plane motion of the coronary arteries during the cardiac cycle: implications for acquisition window duration for MR flow quantification. J Magn Reson Imaging 1998; 8:568–576.
35. Davis P, Crooks L, Arakawa M, McRee R, Kaufmann L, Margulis A. Potential hazards in NMR imaging: heating effects of changing magnetic fields and RF fields on small metallic implants. AJR Am J Roentgenol 1981; 137:857–860.
36. Shellock F. MR imaging of metallic implants and materials: a compilation of the literature. AJR Am J Roentgenol 1988; 151:811–814.
37. Bellon E, Haacke E, Coleman P, Sacco D, Steiger D, Gangarosa R. MR artifacts: a review. AJR Am J Roentgenol 1986; 147: 1271–1281.
38. Heindel W, Friedmann G, Bunke J, Thomas B, Firsching R, Ernestus R. Artifacts in MR imaging after surgical intervention. J Comput Assist Tomogr 1986; 10:596–599.
39. Augustiny N, von Schulthess G, Meier D, Bosiger P. MR imaging of large nonferromagnetic metallic implants at 1.5 T. J Comput Assist Tomogr 1987; 11:678–683.
40. Lüdecke KM, Roeschmann P, Tischler R. Susceptibility artifacts in NMR imaging. J Magn Reson Imaging 1985; 3:329–343.